RSC Advances

PAPER

View Article Online
View Journal | View Issue

Cite this: *RSC Adv.*, 2017, **7**, 27397

Self-template synthesis of $ATiO_3$ (A = Ba, Pb and Sr) perovskites for photocatalytic removal of NO†

Shiyi Cai,‡[ab] Shan Yu,‡[b] Wenchao Wan,[b] Wen Wen[c] and Ying Zhou *[ab]

Received 27th February 2017
Accepted 5th May 2017

DOI: 10.1039/c7ra02433a

rsc.li/rsc-advances

In this study, we report a self-template hydrothermal method for the synthesis of $ATiO_3$ (A = Ba, Pb, and Sr) perovskites using anatase TiO_2 nanosheets as precursors. Under hydrothermal conditions, $ATiO_3$ with different structures and morphology can be obtained. These samples were characterized by X-ray diffraction (XRD), scanning electron microscopy (SEM) and transmission electron microscopy (TEM) techniques. The growth mechanism of $ATiO_3$ was explored by XRD evaluation over different reaction time, and it was observed that $PbTiO_3$ grows most slowly among all the samples including $BaTiO_3$, $SrTiO_3$, $Ba_xPb_{1-x}TiO_3$ and $Sr_xPb_{1-x}TiO_3$. The diffusion of A site sources to the solid surface and the reaction at solid/liquid interface could dominate the growth of $ATiO_3$. All the as-prepared samples exhibited activities toward photocatalytic oxidation of NO at ppb level. Specifically, $PbTiO_3$ has revealed the highest activity under both full spectrum and visible-light irradiation (λ > 420 nm), whereas $BaTiO_3$ exhibited best selectivity for the formation of ionic species (NO_3^-), which could be ascribed to different electronic structures and charge separation efficiency of $ATiO_3$. This study provides some important hints to tune the photocatalytic performances (activity and selectivity) of $ATiO_3$ through the modification of A site elements.

1. Introduction

Photocatalytic solar-energy conversion has attracted extensive attention as one of the ideal technologies for dealing with global energy crisis and environmental pollution.[1–3] Although a variety of new type photocatalysts have been discovered over past years,[4–6] TiO_2 is one of the most intensively investigated and widely used photocatalysts due to its photostability and high efficiency.[7–9] To date, much effort has been made to synthesize TiO_2 with different morphologies such as nanowires, nanosheets, nanocubes and nanotubes to meet the requirements of specific applications.[10–12] Interestingly, the prepared nanostructured TiO_2 can be used as a self-template to obtain complex Ti-based composites.[13,14] For instance, we have successfully prepared photocatalytically active $SrTiO_3$ nanocrystals using anatase TiO_2 nanosheets as the precursor.[15] Therefore, this self-template approach offers a new chance to tune the composition, electronic structure and the resulting photocatalytic performance of Ti-based composites.

$ATiO_3$ (A = Ba, Sr, Pb) typical perovskite-type oxides have been investigated intensively due to their wide applications in gas sensors, capacitors, actuators and photoelectrodes for dye-sensitized solar cells.[16–19] With respect to photocatalysis, Yin *et al.* found that octahedral-shaped perovskite $PbTiO_3$ nanocrystals can degrade methylene blue (MB) efficiently under visible light irradiation.[20] Kimijima *et al.* compared the photocatalytic hydrogen efficiency of cubic, spherical and flake-type $SrTiO_3$ particles.[21] Dunn *et al.* ascribed the enhanced photocatalytic activity of $BaTiO_3$ to the ferroelectricity of its tetragonal phase.[22] It is worth noting that the photocatalytic performances of $ATiO_3$ can be further enhanced by the formation of a heterojunction such as $BaTiO_3/Cu_2O$,[23] $BaTiO_3/TiO_2$,[24] and $BaTiO_3/Bi_2O_3$.[25] Moreover, on combining Ag nanoparticles, $SrTiO_3$ showed a relatively high photocatalytic efficiency for the degradation of NO_x at ppb levels, which is one of the major pollutants in air.[26] However, while there are numerous reports on photocatalytic performances of individual $ATiO_3$, very limited study has been conducted on the effects of different elements in A site on the photocatalytic performances. Nevertheless, it is believed that a series of Ti-based perovskites could be synthesized with the same TiO_2 precursor and the corresponding A site element source. With respect to this strategy,

[a]State Key Laboratory of Oil and Gas Reservoir Geology and Exploitation, Southwest Petroleum University, Chengdu 610500, China. E-mail: yzhou@swpu.edu.cn
[b]The Center of New Energy Materials and Technology, School of Materials Science and Engineering, Southwest Petroleum University, Chengdu 610500, China
[c]Shanghai Synchrotron Radiation Facility, Shanghai Institute of Applied Physics, Chinese Academy of Science, Shanghai 201204, China

† Electronic supplementary information (ESI) available: EDXS elemental mapping of $Ba_xPb_{1-x}TiO_3$ and $Sr_xPb_{1-x}TiO_3$, nitrogen adsorption–desorption tests as well as the pore diameter of $ATiO_3$, XRD patterns of $PbTiO_3$ measured at different reaction time, photocatalytic removal of NO and evolution of NO_2 by TiO_2 under full spectrum illumination, and by $ATiO_3$ under visible light irradiation. See DOI: 10.1039/c7ra02433a

‡ These authors contributed equally to this work and should be considered co-first authors.

the influence of different A site elements in $ATiO_3$ on their photocatalytic activity could be studied.[27,28]

In the present study, we synthesized a series of $ATiO_3$ (A = Ba, Sr and Pb) perovskites by self-template method using anatase TiO_2 nanosheets mainly exposed with {001} facet as the precursor. The influence of A site elements on the structure, morphology, growth kinetics of the $ATiO_3$ samples was studied. Moreover, photocatalytic oxidation of NO over these $ATiO_3$ perovskites shows that the photocatalytic activity and selectivity are strongly related to their electronic structure and charge separation efficiency, which can be supported by electrochemical and photoelectrochemical measurements. It is expected that this study could offer some details on the effect of different A site elements on the photocatalytic performances of perovskites-type titanate oxides.

2. Experimental

2.1 Hydrothermal synthesis of $ATiO_3$ (A = Ba, Pb, and Sr)

TiO_2 nanosheets dominated with {001} facets were first synthesized according to the previously reported hydrothermal method.[15,29,30] Then, 5 mmol of the as-synthesized anatase TiO_2 nanosheets and 2.5 mmol of $Ba(OH)_2\cdot 8H_2O$ or $Pb(NO_3)_2$ or $Sr(OH)_2\cdot 2H_2O$ were dispersed in 15 mL deionized water. $Sr_xPb_{1-x}TiO_3$ and $Ba_xPb_{1-x}TiO_3$ with the introduction of Pb atom on the A site of $SrTiO_3$ and $BaTiO_3$ were also synthesized similarly through the addition of 2.5 mmol of $Sr(OH)_2\cdot 2H_2O$ or $Ba(OH)_2\cdot 8H_2O$: 2.5 mmol of $(Pb(NO_3)_2$ and 5 mmol TiO_2 nanosheets. After adjusting the pH value of the system to 14 by KOH aqueous solution (12 M), the mixture was transferred into a 50 mL Teflon-lined vessel and heated to 140 or 160 °C with different reaction time periods of 2, 4, 6, 8, 24 and 72 h. After reaction, the obtained products were filtered and washed with deionized water and finally dried at 50 °C for 24 h in air.

2.2 Characterization

Synchrotron X-ray diffraction (XRD) experiments were performed at the beamline BL14B1 of Shanghai Synchrotron Radiation Facility (SSRF) with the transmittance mode at a wavelength of 0.6887 Å. Scanning electron microscopy (SEM) and energy dispersive X-ray spectroscopy (EDXS) were measured on an EVOMA 15 microscope equipped with an EDAX detector. Transmission electron microscopy (TEM), high-resolution TEM (HRTEM) and selected area electron diffraction (SAED) images were recorded on a FEI Tecnai G2 20 microscopy operated at 200 kV. Nitrogen adsorption–desorption isotherms were generated on a nitrogen adsorption apparatus (Quantachrome) and all the samples were degassed at 150 °C for 4 h. UV-Vis diffuse reflectance spectra were obtained by a Shimadzu 2600 UV-Vis spectrometer using $BaSO_4$ as the reflectance standard reference.

2.3 Photocatalytic activity evaluation

Photocatalytic performance was evaluated through the photocatalytic removal of NO at ppb level in a continuous flow reactor at room temperature. Details of the reactor set-up can be referred from the previous study.[3] Typically, a 150 W commercial metal halide lamp (ZY73-TD150/At, Yaming) was used as the light source and horizontally placed above the reactor (30 cm × 15 cm × 10 cm). The light intensity reaching the surface of the photocatalyst was measured as 51.3 mW cm^{-2} at 535 nm using a photometer (PM100D, Thorlabs). The catalysts (60 mg, grinded and sieved to 100–200 μm grains before use) were uniformly dispersed in two Petri dishes with a diameter of 12.0 cm in the center of the reactor. The flow rate of air and NO was 1.51 L min^{-1} and 12.1 mL min^{-1} during the tests, respectively. The concentration of NO before illumination was 700 ppb. The real-time concentration of NO and NO_x (which could be seen as the molecular mixture of NO and NO_2) was monitored by a NO_x analyzer (Thermo Scientific, 42i-TL). The ratio of NO removal (η_1%) and NO_2 generation (η_2%) can be given by following equations:[26,31]

$$\eta_1\% = \left(1 - \frac{C_{(NO)}}{C_{0(NO)}}\right) \times 100\% \quad (1)$$

$$\eta_2\% = \frac{C_{(NO_x)} - C_{(NO)} - \left(C_{0(NO_x)} - C_{0(NO)}\right)}{C_{(NO_x)}} \times 100\% \quad (2)$$

where $C_{0(NO)}$ and $C_{0(NO_x)}$ are the initial concentrations of NO and NO_x, respectively, before illumination, and $C_{(NO)}$ and $C_{(NO_x)}$ are the real-time concentrations of NO and NO_x, respectively, during photocatalysis. Based on this, the initial and real-time concentrations of NO_2 can be calculated as $(C_{0(NO_x)} - C_{0(NO)})$ and $(C_{(NO_x)} - C_{(NO)})$ respectively. Therefore, the remaining ratio of NO at a given time was noted as $C_{(NO)}/C_{0(NO)}$, and the generated amount of NO_2 during the reaction could be written as $[C_{(NO_x)} - C_{(NO)} - (C_{0(NO_x)} - C_{0(NO)})]$.

2.4 Electrochemical and photoelectrochemical measurement

Electrochemical and photoelectrochemical measurements were performed on a CHI 660 electrochemical workstation with a standard three-electrode cell system, in which platinum wire, standard calomel electrode (SCE) and 0.5 M Na_2SO_4 solution were employed as the counter electrode, reference electrode and electrolyte, respectively. Working electrode was prepared by the following process: 20 mg of the prepared $ATiO_3$ was mixed with 0.5 mL of ethanol and 0.5 mL of water, and the mixture was ground thoroughly and laid on the fluorine-doped tin oxide (FTO) by the doctor-blade method. The decorated FTO was then annealed at 250 °C for 4 h with a heating rate of 80 °C h^{-1} to achieve the fabrication of the working electrode. Light irradiation was provided by a 300 W Xe lamp with the intensity of 246.0 mW cm^{-2}.

3. Results and discussion

3.1 Crystal structure and morphology

Fig. 1 shows the XRD patterns of $BaTiO_3$, $SrTiO_3$, $PbTiO_3$ and their composites prepared at 160 °C for 24 h. Basically, the diffraction peaks are indexed to the tetragonal structure of $BaTiO_3$ (JCPDS 05-0626, $\alpha = b = 3.994$ Å, $c = 4.038$ Å), $PbTiO_3$ (JCPDS 06-0452, $\alpha = b = 3.899$ Å, $c = 4.153$ Å) and cubic

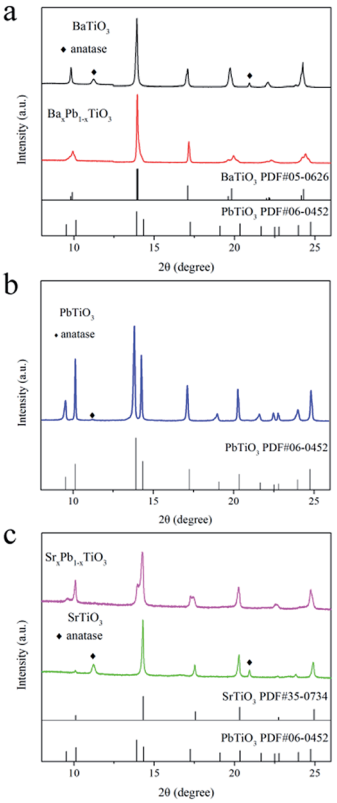

Fig. 1 XRD patterns of the $ATiO_3$ prepared at 160 °C for 24 h: (a) $BaTiO_3$ and $Ba_xPb_{1-x}TiO_3$; (b) $PbTiO_3$; (c) $Sr_xPb_{1-x}TiO_3$ and $SrTiO_3$.

structure of $SrTiO_3$ (JCPDS 35-0734, $\alpha = b = c = 3.905$ Å), respectively. It is worth noting that several additional diffraction peaks related to anatase TiO_2 could also be observed (diamond symbol in Fig. 1a and c) due to the excessive amount of TiO_2 precursor in the system (the molar ratio of Ti source to A (Ba, Sr, or Pb) source is 2 : 1). In addition to $ATiO_3$ with single element of A site, we also introduced Pb atom in $BaTiO_3$ and $SrTiO_3$ to prepare $Ba_xPb_{1-x}TiO_3$ and $Sr_xPb_{1-x}TiO_3$. Due to the introduction of Pb atom in $BaTiO_3$, crystal defects were formed, thereby broadening the diffraction peaks of $Ba_xPb_{1-x}TiO_3$ when compared to $BaTiO_3$ (Fig. 1a), but the position of the peaks was almost similar to that of $BaTiO_3$. However, for $Sr_xPb_{1-x}TiO_3$, the diffraction peaks of $PbTiO_3$ could be clearly found in addition to the diffraction peaks of $SrTiO_3$ (club symbol in Fig. 1c). In general, the formation of solid solution between two materials depends on their matching extent in several factors such as crystal structure, electronegativity and chemical valence. For instance, the ionic radius of the two elements should be close to each other (with a difference less than 15%).[32] This is particularly important for $ATiO_3$, as each atom on A site is highly coordinated with 12 nearby oxygen atoms. The ionic radii of Sr, Ba and Pb are 1.44, 1.61 and 1.49 Å, respectively. The difference between them was within 15%, indicating that the generation of the solid solution from $BaTiO_3$ or $SrTiO_3$ and $PbTiO_3$ was possible. In addition, the electronegativity and chemical valence of these three atoms were similar as well. Nevertheless, it should be noted that a similar crystal structure of these materials was also necessary for the formation of a solid solution. $SrTiO_3$ has a different cubic crystal structure from $BaTiO_3$ and $PbTiO_3$, and both the latter have a similar tetragonal structure. Therefore, a solid solution ($Ba_xPb_{1-x}TiO_3$) was obtained from $BaTiO_3$ and $PbTiO_3$ (*cf.* Fig. 1a), whereas $SrTiO_3$ and $PbTiO_3$ tended to form a composite ($Sr_xPb_{1-x}TiO_3$), as evidenced from the XRD pattern (Fig. 1c).

Typical SEM images (Fig. 2) revealed that all the samples have a nanostructure in the range of tens to hundreds of nanometers. Specifically, $BaTiO_3$ is mainly present as piled-up pellets from 40 to 200 nm (Fig. 2a). In contrast, the packing of $Ba_xPb_{1-x}TiO_3$ is more compact and the pellets tend to convert into polygon-shaped sheets (Fig. 2b). Moreover, the morphology of $PbTiO_3$ is different from that of $BaTiO_3$ and instead, the formation of 2D nanosheets is observed (Fig. 2c). Among all the samples, $Sr_xPb_{1-x}TiO_3$ (Fig. 2d) possesses the most uniform morphology, composed of cubic nanoparticles of the size of about 40 nm. However, this uniformity disappears for $SrTiO_3$: cubic particles from 40 to 400 nm can be found in the SEM image (Fig. 2e). Clearly, the substitution of A site atom in $ATiO_3$ has a significant influence on the morphology of the final products. Furthermore, EDXS results (Fig. 2f and g) reveal the existence of Pb atom in $Ba_xPb_{1-x}TiO_3$ solid solution and $Sr_xPb_{1-x}TiO_3$ composite, and these elements have uniform distribution, as evidenced by elemental mappings (Fig. S1†).

To further investigate the morphology and microstructure of these samples, TEM studies were carried out. As shown in Fig. 3a, $BaTiO_3$ nanoparticles are close to round-shape. HRTEM image (Fig. 3b) of $BaTiO_3$ indicates a lattice spacing of 0.284 nm,

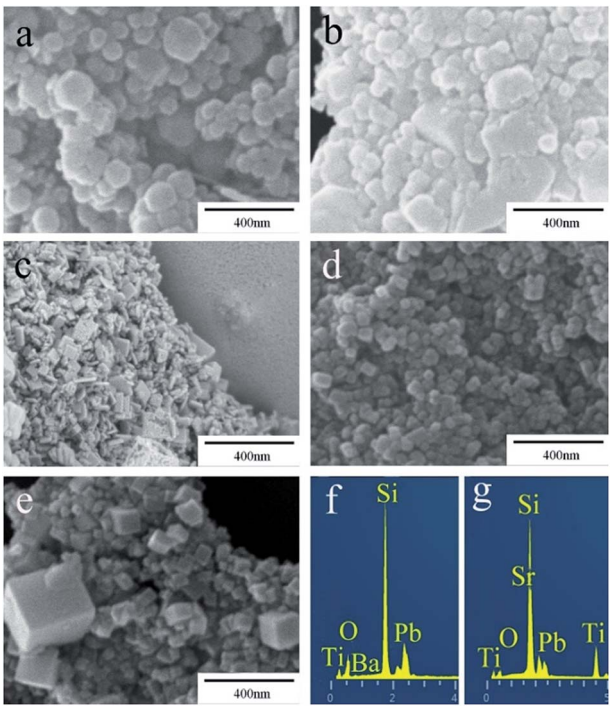

Fig. 2 Typical SEM images of $ATiO_3$: (a) $BaTiO_3$, (b) $Ba_xPb_{1-x}TiO_3$, (c) $PbTiO_3$, (d) $Sr_xPb_{1-x}TiO_3$, (e) $SrTiO_3$, and EDXS of (f) $Ba_xPb_{1-x}TiO_3$ and (g) $Sr_xPb_{1-x}TiO_3$.

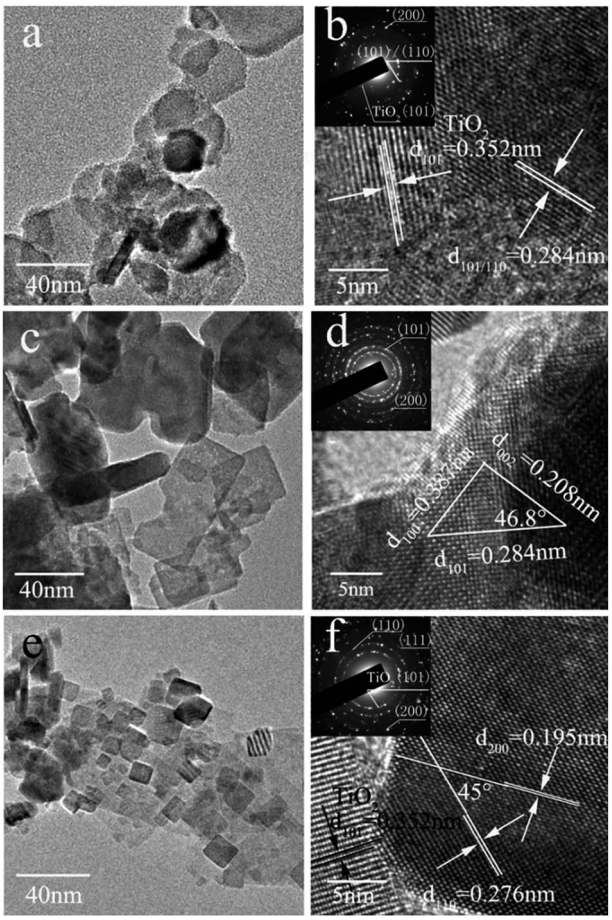

Fig. 3 TEM and HRTEM images of $ATiO_3$ (inset is the corresponding SAED pattern): (a and b) $BaTiO_3$, (c and d) $PbTiO_3$, (e and f) $SrTiO_3$.

which corresponds to (101) or (110) planes of $BaTiO_3$. This is further confirmed by the SAED pattern. For $PbTiO_3$, the TEM image (Fig. 3c) confirms the sheet shaped morphology. These nanosheets are very thin and are transparent under the electron beam. In addition, the lattice spacing of 0.208, 0.284 and 0.387 nm with contact angle of 46.8° and 90° in the triangle region can be clearly observed (Fig. 3d), which matches well with the (002), (101), (100) planes of $PbTiO_3$, respectively. In accordance with the SEM results (*cf.* Fig. 2), the morphology of $SrTiO_3$ was relatively regular (Fig. 3e). Two crystal planes with lattice spacing of 0.276 and 0.195 nm and a contact angle of 45° are attributed to the (110) and (200) planes of $SrTiO_3$ (Fig. 3f). In combination with the XRD results (Fig. 3), it is clear that this self-template method can be applied to synthesize perovskite-type $ATiO_3$ with various A site elements. Moreover, TEM investigation indicated that the anatase TiO_2 precursor is residual in $SrTiO_3$ and $BaTiO_3$ because the characteristic crystal fringes of anatase TiO_2 were observed in their HRTEM images (Fig. 3b and f), which agrees well with the XRD results. Fig. S2† shows the nitrogen adsorption–desorption isotherms as well as the corresponding pore volume of these samples. All of them revealed a typical type of H4 hysteresis loop (Fig. S2f†), which is often ascribed to the narrow slit-like pores.[33] The determined specific surface area (S_{BET}) of $BaTiO_3$, $PbTiO_3$ and $SrTiO_3$ is 33.4, 40.1 and 52.1 $m^2\ g^{-1}$, respectively. Specifically, the substitution of Ba and Sr with Pb atom and the formation of solid solution (Ba_x-$Pb_{1-x}TiO_3$) and composite ($Sr_xPb_{1-x}TiO_3$) led to the decrease of surface area and pore volume. The detailed surface area and pore parameters of these samples are shown in Table 1. These results demonstrate that the element in A site not only affects the structure and morphology of $ATiO_3$, but also modifies their surface area and pore size.

3.2 Hydrothermal growth process

In order to understand the hydrothermal growth process of these $ATiO_3$ perovskites, we measured the XRD patterns of the products over different reaction times. Fig. S3† shows typical XRD patterns for the growth of $PbTiO_3$ at 160 °C. No diffraction patterns of intermediate other than $PbTiO_3$ and anatase TiO_2 precursor were detected during the entire test time (72 h). As time increases, the diffraction peaks of $PbTiO_3$ become sharp, while that of anatase TiO_2 become weaker. Similar phenomenon was observed for $BaTiO_3$ and $SrTiO_3$ as well. Then, on assuming that the entire reaction has been completed at 72 h, kinetic analysis could be performed by fitting the data of the most intense reflection (101) of $BaTiO_3$ and (110) of $PbTiO_3$ and $SrTiO_3$ to the expression which correlates the extent of reaction (α) to time.[34–38] Fig. 4 reveals the variations of α values of $BaTiO_3$, $PbTiO_3$ and $SrTiO_3$ over time at different temperatures. The growth of $BaTiO_3$ and $SrTiO_3$ is relatively fast (in minutes), whereas the kinetics of $PbTiO_3$ is the slowest among the studied samples. These results reveal the sensitive response of the $ATiO_3$ growth process to the alteration of only A site elements. Furthermore, on increasing the reaction temperature from 140 to 160 °C, the leads to a reduction of the half-life time $t_{0.5}$ of these samples, indicating that increasing the temperature can accelerate these reactions, which is consistent with our previous study on the hydrothermal growth of Bi_2WO_6.[39]

A much detailed description of kinetic evaluation can be obtained through the Sharp–Hancock (SH) plots,[40–43] where $\ln[-\ln(1-\alpha)]$ *versus* $\ln(t)$ is plotted. The reaction mechanistic change can be indicated from a change in the slope of the SH curve. Moreover, the reaction exponent (m) can be determined from the linear region of this curve. It is extremely difficult to perform a detailed and rigorous analysis due to the limited available data (Fig. 4), particularly for the growth of $BaTiO_3$ and $SrTiO_3$ given the rapid reaction speed. However, such analysis could provide insights into the influence of A site elements on the corresponding hydrothermal growth process.

Table 1 BET surface area, pore parameters

Sample	S_{BET}/$m^2\ g^{-1}$	Pore volume/ $cm^3 \cdot g^{-1}$	Pore size/nm
$BaTiO_3$	33.4	0.168	19.4
$Ba_xPb_{1-x}TiO_3$	9.2	0.057	14.4
$PbTiO_3$	40.1	0.127	11.1
$Sr_xPb_{1-x}TiO_3$	20.5	0.107	19.5
$SrTiO_3$	52.1	0.218	14.9

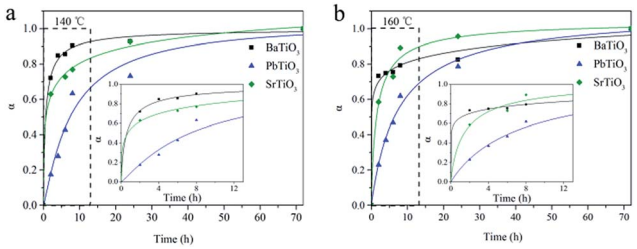

Fig. 4 Extent of reaction (α) of $ATiO_3$ as a function of the reaction time at (a) 140 °C and (b) 160 °C. Inset is the enlarged view from the dotted line region.

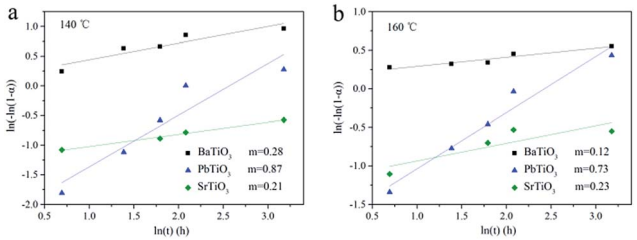

Fig. 5 Johnson–Mehl Avrami plots for $ATiO_3$ at different reaction temperature (a) 140 °C and (b) 160 °C.

Fig. 5 shows the SH plot of $BaTiO_3$, $SrTiO_3$ and $PbTiO_3$ obtained at different reaction temperatures. It can be observed that $BaTiO_3$ and $SrTiO_3$ with $m \approx 0.2$ exhibited a completely different reaction mechanism from $PbTiO_3$ with $m \approx 0.8$. Importantly, the growth mechanism of $ATiO_3$ was temperature independent given that m varies little from 140 to 160 °C. In general, $m \approx 0.5$ has indicated a diffusion-controlled process, whereas $m \approx 1.0$ has revealed a phase-boundary controlled growth mechanism.[42] Therefore, the growth of $BaTiO_3$ and $SrTiO_3$ seemed to be controlled by diffusion process, while the growth of $PbTiO_3$ with $m \approx 0.8$ was more in accordance with diffusion-controlled and/or a phase-boundary controlled process. In the current hydrothermal reaction, as we have used solid TiO_2 nanosheets as the precursor, diffusion of A site sources to the solid surface and the reaction at the solid/liquid interface could dominate the growth of $ATiO_3$, which is similar to the hydrothermal growth of $Bi_6S_2O_{15}$ nanowire using Bi_2O_3 particles as the precursor.[44]

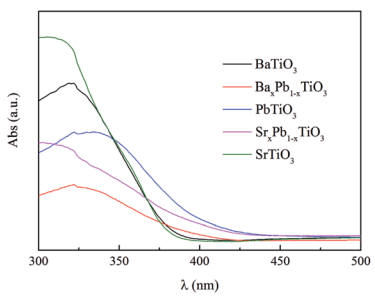

Fig. 6 UV-Vis diffuse reflectance spectra of $ATiO_3$.

3.3 Optical property and photocatalytic performance

Fig. 6 shows the UV-Vis diffuse reflection spectra (DRS) of these samples. Both $BaTiO_3$ and $SrTiO_3$ have a similar absorption edge starting at about 390 nm, suggesting that they are only responsive to UV light, while $PbTiO_3$ is responsive to visible light with wavelength of 425 nm. The addition of Pb into $BaTiO_3$ and $SrTiO_3$ can enhance their light absorption in visible region. Therefore, the band gap (E_g) of $BaTiO_3$, $Ba_xPb_{1-x}TiO_3$, $PbTiO_3$, $Sr_xPb_{1-x}TiO_3$ and $SrTiO_3$ is determined to be 3.22, 3.02 3.00, 2.95 and 3.22 eV, respectively, according to the onset of the absorption edge (*cf.* Table 2).

The photocatalytic activities of these samples were evaluated through photocatalytic oxidation of NO at an indoor air level (700 ppb). NO generated from the combustion of fossil fuels is one of the main sources causing acid rain and photochemical smog. Traditional methods for disposal of NO include physical adsorption, biofiltration, and thermal catalysis. In comparison, photocatalytic decomposition of NO has advantages like low energy consumption, removal of low concentration of NO and environmental friendliness. Before illumination, the samples were exposed to continuous NO gas flow for 30 min to reach the adsorption–desorption equilibrium. Under full spectrum irradiation, all of them exhibited photocatalytic activity toward NO oxidation: the concentration of NO decreases rapidly within the first 5 min after illumination and then becomes stable for all samples (Fig. 7). Particularly, $PbTiO_3$ presents the highest NO removal efficiency of 43%, followed by $SrTiO_3$ (40%) and $BaTiO_3$ (30%), whereas the removal efficiency for both $Ba_xPb_{1-x}TiO_3$ and $Sr_xPb_{1-x}TiO_3$ is only approximately 20%. Control experiments show that the remaining TiO_2 nanosheet in $ATiO_3$ also has some photocatalytic activity for the degradation of NO (Fig. S4†); however, it should not be the main source of the photocatalytic activity in the $ATiO_3$ samples, judging from their low content in the samples and the uncorrelated activity with the remaining amount of TiO_2. In addition, $PbTiO_3$ reveals stable photocatalytic activity reflected from the recycling experiments. As shown in Fig. 8, after running five cycles, NO removal ratio over $PbTiO_3$ can still reach *ca.* 40% under full spectrum irradiation, while other samples showed different degrees of attenuation. Given that $Ba_xPb_{1-x}TiO_3$, $PbTiO_3$ and $Sr_xPb_{1-x}TiO_3$ are responsive to visible light (*cf.* Fig. 6), the visible light driven photocatalytic activities of all the samples were evaluated as well. With respect to optical absorption, $Ba_xPb_{1-x}TiO_3$, $PbTiO_3$ and $Sr_xPb_{1-x}TiO_3$ are more active under visible light irradiation than $SrTiO_3$ and $BaTiO_3$ (Fig. S5a†), as neither of them can absorb visible light. Furthermore, the

Table 2 The band structures of $ATiO_3$

Sample	Band gap/eV	CB/eV	VB/eV
$BaTiO_3$	3.22	−0.799	2.421
$Ba_xPb_{1-x}TiO_3$	3.02	−1.026	1.994
$PbTiO_3$	3.00	−0.928	2.072
$Sr_xPb_{1-x}TiO_3$	2.95	−1.051	1.899
$SrTiO_3$	3.22	−0.881	2.339

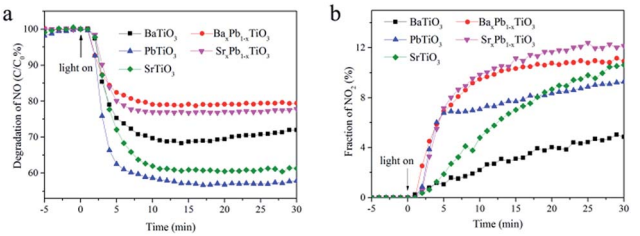

Fig. 7 Concentration changes of NO (a) and NO_2 (b) in the presence of $ATiO_3$ under irradiation. Light source: 150 W commercial tungsten halogen lamp; flowing rate of air: 1.51 L min^{-1}; flowing rate of NO: 12.1 mL min^{-1}.

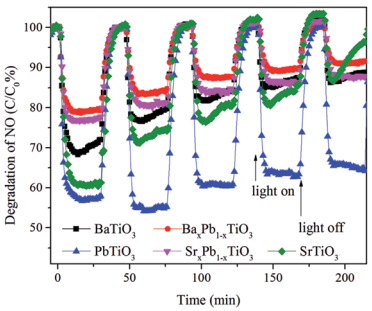

Fig. 8 Recycling runs of photocatalytic oxidation of NO over $PbTiO_3$ under full spectrum irradiation.

monitoring of the intermediates (selectivity) could be equally important with the activity because the intermediates (NO_2) are also harmful to human health. The desired oxidation products should be the ionic species (NO_3^-) as they can be washed away. Therefore, the concentration of the incomplete NO oxidation product, NO_2, is an important evaluation standard during the photocatalytic process. Usually, the weaker the oxidation ability of the photogenerated holes is, the larger the concentration of NO_2 will be. NO_2 was monitored online under both full spectrum and visible light irradiation as shown in Fig. 7b and 5b. Regardless of the light sources, the fraction of NO_2 generated over $SrTiO_3$ and $BaTiO_3$ was remarkably lower than that over other samples, which indicates that $SrTiO_3$ and $BaTiO_3$ could possess stronger oxidation ability and promote the oxidation of NO_2 to final NO_3^-.[3] From Fig. 7, we noted that the oxidation ability order ($Sr_xPb_{1-x}TiO_3$ < $Ba_xPb_{1-x}TiO_3$ < $PbTiO_3$ < $SrTiO_3$ < $BaTiO_3$) is quite different from the activity order ($Ba_xPb_{1-x}TiO_3$ < $Sr_xPb_{1-x}TiO_3$ < $BaTiO_3$ < $SrTiO_3$ < $PbTiO_3$). These results demonstrate that not only the activity but also the selectivity of $ATiO_3$ could be tuned through the modification of A site elements.

3.4 Electrochemical and photoelectrochemical measurements

In general, the photocatalytic performance is mainly governed by three processes: light absorption, charge separation and migration, and surface redox potential. Clearly, the different photocatalytic activity of $ATiO_3$ could not be solely attributed to BET surface area (*cf.* Table 1). In addition, the charge separation and migration as well as surface redox potential could play important roles in this system.

Mott–Schottky (MS) curve was then analysed to determine the surface redox potential of the samples.[45] As shown in Fig. 9a, all the $ATiO_3$ samples exhibited MS curve with anti-S type and positive slope in the linear region, illustrating that they are n-type semiconductors. Therefore, the flat band potential (E_{fb}) could be an indication of the position of the conduction band edge (E_{CB}) for $ATiO_3$, which was obtained from the interception of tangent in the linear region. Combined with the band gap value calculated from the UV-Vis DRS data (Fig. 6), we can determine the exact position of the conduction band edge and the valence band edge (E_{VB}) of $ATiO_3$ (Fig. 9b and Table 2). The value of E_{VB} for $ATiO_3$ increased in the following order: $Sr_xPb_{1-x}TiO_3$ < $Ba_xPb_{1-x}TiO_3$ < $PbTiO_3$ < $SrTiO_3$ < $BaTiO_3$, and matched with the order of the generated fraction of NO_2 (Fig. 7b). A less positive valence band position often indicates weaker oxidation ability and hence a larger amount of incomplete oxidation product, NO_2.

Fig. 10a shows the transient photocurrent response of $ATiO_3$ under periodical light on–off cycles. All the $ATiO_3$ samples present positive current with light-on, further confirming that they are n-type semiconductors. Though a photocurrent spike occurs immediately after illumination for $PbTiO_3$, the photocurrent generated by $PbTiO_3$ is still much stronger than others and the transient photocurrent is well maintained (with a photocurrent intensity of *ca.* 0.6 μA cm^{-2}) after 10 on–off cycles. In contrast, the photocurrent obtained from $Sr_xPb_{1-x}TiO_3$ and $Ba_xPb_{1-x}TiO_3$ is smaller than 0.2 μA cm^{-2}. For $SrTiO_3$ and $BaTiO_3$, their corresponding photocurrent is very close to each other in the beginning; however, the photocurrent decay for $BaTiO_3$ is more prominent. These results demonstrate that the charge separation efficiency is the highest for $PbTiO_3$ and lowest for $Sr_xPb_{1-x}TiO_3$ and $Ba_xPb_{1-x}TiO_3$, and charge separation efficiency of $SrTiO_3$ should be higher than that of $BaTiO_3$. These results are further confirmed by electrochemical impedance spectroscopy (EIS) investigations (Fig. 10b): the resistance of $PbTiO_3$ is much smaller than that of $Sr_xPb_{1-x}TiO_3$, $Ba_xPb_{1-x}TiO_3$ and $BaTiO_3$ is the largest. Both the photocurrent and EIS results agree well with the order of photocatalytic activity ($Ba_xPb_{1-x}TiO_3$ < $Sr_xPb_{1-x}TiO_3$ < $BaTiO_3$ < $SrTiO_3$ < $PbTiO_3$) (*cf.* Fig. 7a). These results demonstrated that the photocatalytic activity of $ATiO_3$ is mainly determined by charge separation

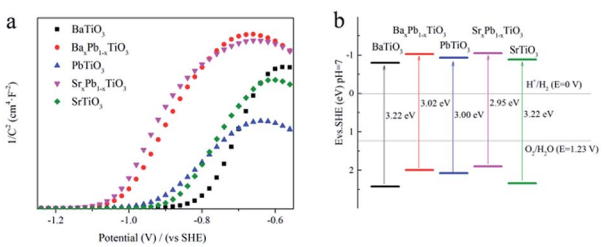

Fig. 9 (a) MS plots (*vs.* SHE) and (b) schematic illustration of the band gap structures (*vs.* SHE) of $ATiO_3$.

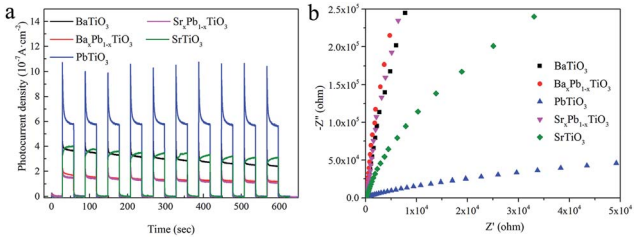

Fig. 10 (a) Transient photocurrent *versus* time and (b) electrochemical impedance tests of $ATiO_3$ (in dark).

efficiency. With the highest charge separation efficiency, more photogenerated holes could migrate to the surface of $PbTiO_3$ and participate in the oxidation of NO, which results in the highest removal proportion of NO.

4. Conclusions

In this study, $ATiO_3$ (A = Pb, Sr and Ba) with perovskite-type oxides has been successfully synthesized *via* a hydrothermal and self-template method from anatase TiO_2 nanosheet precursor. Under the same reaction conditions, $BaTiO_3$, $PbTiO_3$ and $SrTiO_3$ nanoparticles could be obtained with round-shaped, nanosheet and cubic morphology, respectively. Dynamics analysis shows that the crystallization of $PbTiO_3$ is much slower than that of $SrTiO_3$ and $BaTiO_3$, and the growth mechanism of $ATiO_3$ is temperature independent in the interval from 140 to 160 °C. Under light illumination, $PbTiO_3$ shows higher photocatalytic activities than others for NO removal, whereas $BaTiO_3$ yields less amount of NO_2 during the process. These are closely related to their electronic structure and charge separation efficiency, as evidenced from the electrochemical and photoelectrochemical measurements. These results demonstrate that both the photocatalytic activity and selectivity of $ATiO_3$ could be tuned through the modification of A site elements.

Acknowledgements

Financial support from the Large Scientific Apparatus Joint Funds of the National Natural Science Foundation of China (U1232119), Sichuan Youth Science and Technology Foundation (2014JQ0017) and the Innovative Research Team of Sichuan Province (2016TD0011) is gratefully acknowledged. We thank SSRF for beamtime at beamline BL14B1.

Notes and references

1 M. Anpo, T. H. Kim and M. Matsuoka, *Catal. Today*, 2009, **142**, 114–124.
2 K. Shimura and H. Yoshida, *Energy Environ. Sci.*, 2011, **4**, 2467–2481.
3 W. C. Wan, S. Yu, F. Dong, Q. Zhang and Y. Zhou, *J. Mater. Chem. A*, 2016, **4**, 7823–7829.
4 X. B. Chen, L. Liu, P. Y. Yu and S. S. Mao, *Science*, 2011, **331**, 746–750.
5 X. C. Wang, K. Maeda, A. Thomas, K. Takanabe, G. Xin, J. M. Carlsson, K. Domen and M. Antonietti, *Nat. Mater.*, 2009, **8**, 76–80.
6 H. W. Huang, Y. He, Z. S. Lin, L. Kang and Y. H. Zhang, *J. Phys. Chem. C*, 2013, **117**, 22986–22994.
7 A. Fujishima and K. Honda, *Nature*, 1972, **238**, 37–38.
8 H. G. Yang, C. H. Sun, S. Z. Qiao, J. Zou, G. Liu, S. C. Smith, H. M. Cheng and G. Q. Lu, *Nature*, 2008, **453**, 638–641.
9 R. Asahi, T. Morikawa, T. Ohwaki, K. Aoki and Y. Taga, *Science*, 2001, **293**, 269–271.
10 J. H. Wu, S. C. Hao, J. M. Lin, M. L. Huang, Y. F. Huang, Z. Lan and P. J. Li, *Cryst. Growth Des.*, 2008, **8**, 247–252.
11 H. Choi, Y. J. Kim, R. S. Varma and D. D. Dionysiou, *Chem. Mater.*, 2006, **18**, 5377–5384.
12 J. Zhou, G. L. Zhao, B. Song and G. R. Han, *CrystEngComm*, 2011, **13**, 2294–2302.
13 J. Zhang, J. H. Bang, C. C. Tang and P. V. Kamat, *ACS Nano*, 2010, **4**, 387–395.
14 Q. Kuang and S. H. Yang, *ACS Appl. Mater. Interfaces*, 2013, **5**, 3683–3690.
15 J. M. Peng, Y. Zhou, H. Wang, H. R. Zhou and S. Y. Cai, *CrystEngComm*, 2015, **17**, 1805–1812.
16 T. Hara, T. Ishiguro, N. Wakiya and K. Shinozaki, *Mater. Sci. Eng., B*, 2009, **161**, 142–145.
17 J. H. Pan, C. Shen, I. Ivanova, N. Zhou, X. Z. Wang, W. C. Tan, Q. H. Xu, D. W. Bahnemann and Q. Wang, *ACS Appl. Mater. Interfaces*, 2015, **7**, 14859–14869.
18 Y. Kim, H. Han, Y. Kim, W. Lee, M. Alexe, S. Baik and J. K. Kim, *Nano Lett.*, 2010, **10**, 2141–2146.
19 M. Alexe and D. Hesse, *J. Mater. Sci.*, 2006, **41**, 1–11.
20 S. M. Yin, H. Tian, Z. H. Ren, X. Wei, C. Y. Chao, J. Y. Pei, X. Li, G. Xu, G. Shen and G. R. Han, *Chem. Commun.*, 2014, **50**, 6027–6030.
21 T. Kimijima, K. Kanie, M. Nakaya and A. Muramatsu, *Appl. Catal., B*, 2014, **144**, 462–467.
22 Y. F. Cui, J. Briscoe and S. Dunn, *Chem. Mater.*, 2013, **25**, 4215–4223.
23 D. Sharma, S. Upadhyay, V. R. Satsangi, R. Shrivastav, U. V. Waghmare and S. Dass, *Appl. Catal., B*, 2016, **189**, 75–85.
24 L. G. Devi and G. Krishnamurthy, *J. Hazard. Mater.*, 2009, **162**, 899–905.
25 P. R. Ren, H. Q. Fan and X. Wang, *Appl. Phys. A: Mater. Sci. Process.*, 2013, **111**, 1139–1145.
26 Q. Zhang, Y. Huang, L. F. Xu, J. J. Cao, W. K. Ho and S. C. Lee, *ACS Appl. Mater. Interfaces*, 2016, **8**, 4165–4174.
27 W. J. Dong, B. J. Li, Y. Li, X. B. Wang, L. N. An, C. R. Li, B. Y. Chen, G. Wang and Z. Shi, *J. Phys. Chem. C*, 2011, **115**, 3918–3925.
28 Y. Li, X. P. Gao, G. R. Li, G. L. Pan, T. Y. Yan and H. Y. Zhu, *J. Phys. Chem. C*, 2009, **113**, 4386–4394.
29 X. H. Yang, Z. Li, G. Liu, J. Xing, C. Sun, H. G. Yang and C. Li, *CrystEngComm*, 2010, **13**, 1378–1383.
30 X. G. Han, Q. Kuang, M. S. Jin, Z. X. Xie and L. S. Zheng, *J. Am. Chem. Soc.*, 2009, **131**, 3152–3153.
31 M. Ou, D. Fan, Z. Wei and Z. B. Wu, *Chem. Eng. J.*, 2014, **255**, 650–658.

32 K. Janghorban, J. S. Kirkaldy and G. C. Weatherly, *J. Phys.: Condens. Matter*, 2001, **13**, 8661–8676.
33 K. S. W. Sing, D. H. Everett, R. A. W. Haul, L. Moscou, R. A. Pierotti, J. Rouquerol and T. Siemieniewska, *Pure Appl. Chem.*, 1985, **57**, 603–619.
34 A. Michailovski, J. D. Grunwaldt, A. Baiker, R. Kiebach, W. Bensch and G. R. Patzke, *Angew. Chem., Int. Ed.*, 2005, **44**, 5643–5647.
35 Y. Zhou, E. Antonova, Y. H. Lin, J. D. Grunwaldt, W. Bensch and G. R. Patzke, *Eur. J. Inorg. Chem.*, 2012, **5**, 783–789.
36 A. Testino, M. T. Buscaglia, V. Buscaglia, M. Viviani, C. Bottino and P. Nanni, *Chem. Mater.*, 2004, **16**, 1536–1543.
37 J. O. Eckert, C. C. Hung-Houston, B. L. Gersten, M. M. Lencka and R. E. Riman, *J. Am. Ceram. Soc.*, 2005, **79**, 2929–2939.
38 J. Moon, E. Suvaci, A. Morrone, S. A. Costantino and J. H. Adair, *J. Eur. Ceram. Soc.*, 2003, **23**, 2153–2161.
39 Y. Zhou, E. Antonova, W. Bensch and G. R. Patzke, *Nanoscale*, 2010, **2**, 2412–2417.
40 J. D. Hancock and J. H. Sharp, *J. Am. Ceram. Soc.*, 1972, **55**, 74–77.
41 A. S. Shaikh and G. M. Vest, *J. Am. Ceram. Soc.*, 1986, **69**, 682–688.
42 F. Maxim, P. M. Vilarinho, P. Ferreira, I. M. Reaney and I. Levin, *Cryst. Growth Des.*, 2011, **11**, 3358–3365.
43 Y. Zhou, N. Pienack, W. Bensch and G. R. Patzke, *Small*, 2009, **5**, 1978–1983.
44 Y. Zhou, J. D. Grunwaldt, F. Krumeich, K. B. Zheng, G. R. Chen, J. Stotzel, R. Frahm and G. R. Patzke, *Small*, 2010, **6**, 1173–1179.
45 Y. F. Liu, Y. H. Lv, Y. Y. Zhu, D. Liu, R. L. Zong and Y. F. Zhu, *Appl. Catal., B*, 2014, **147**, 851–857.